

Orbital-angular-momentum-resolved electron magnetic chiral dichroism

*Enzo Rotunno¹, Matteo Zanfrognini¹, Stefano Frabboni^{1,2}, Jan Ruzsz³,
Rafal E. Dunin Borkowski⁴, Ebrahim Karimi⁵ and Vincenzo Grillo¹*

1. CNR-NANO via G Campi 213/a, 41125 Modena, Italy
2. Università di Modena e Reggio Emilia, via G. Campi 213/a, 41125, Modena, Italy
3. Department of Physics and Astronomy, Uppsala University, P.O. Box 516, 75120 Uppsala, Sweden
4. Ernst Ruska-Centre for Microscopy and Spectroscopy with Electrons and Peter Grünberg Institute, Forschungszentrum Jülich, 52425 Jülich, Germany
5. Department of Physics, University of Ottawa, 150 Louis Pasteur, Ottawa, Ontario K1N 6N5, Canada

Abstract

We propose a highly efficient atomically-resolved mode of electron magnetic chiral dichroism. This method exploits the recently introduced orbital angular momentum spectrometer to analyze the inelastically scattered electrons allowing for simultaneous dispersion in both energy and angular momentum. The technique offers several advantages over previous formulations of electron magnetic chiral dichroism as it requires much simpler experimental conditions in terms of specimen orientation and thickness.

A novel simulation algorithm, based on the multislice description of the beam propagation, is used to anticipate the advantages of the new approach over current electron magnetic chiral dichroism implementations. Numerical calculations confirm an increased magnetic signal to noise ratio with in plane atomic resolution.

Introduction

Since its first experimental demonstration [1], electron magnetic chiral dichroism (EMCD) has attracted great interest in physics and materials science because it offers the potential to study the magnetic properties of materials in the transmission electron microscope (TEM) with atomic spatial resolution [2]. In the earliest formulation of EMCD proposed by Schattschneider et al. [1, 3], the measurement of a dichroic signal is based on the use of a parallel electron beam, a two (or three) beam orientation of the crystalline sample and the recording of electron energy-loss (EEL) spectra at two specific positions in the diffraction plane. The drawbacks to this approach include limited spatial resolution [4] (typically several nm), poor signal-to-noise ratio (SNR) and a strong dependence of the strength of the dichroic signal on sample thickness, with numerical simulations in Ref. [3] reporting that the signal can be close to zero at some sample thicknesses. Whereas the principle of the technique relies on the detection of a change in the orbital angular momentum of the inelastically scattered wave, its standard formulation only makes use of post-selection of the scattered momentum.

A recent advance in electron microscopy has involved the introduction of electron vortex beams [5, 6, 7], including the possibility to create atomic-sized electron vortices [8, 9]. Electron beams that have a given topological charge can in principle be focused onto a single atomic column and induce atomic excitations, with different intensities for transitions in which the magnetic quantum number changes by $\Delta m = \pm 1$. [10] For example, for $2p \rightarrow 3d$ transitions in magnetic transition metals differences in energy-resolved diffraction patterns are expected for vortices with opposite orbital angular momentum (OAM) of $\pm \hbar$ because of the different populations of spin-up and spin-down $3d$

electronic states. [11,12,13] Unfortunately, this approach is difficult for three reasons. First, it requires two measurements using opposite electron vortex beams (typically with $l = +1$ and $l = -1$), which cannot easily be performed on exactly the same region due to sample and probe drift. Second, an electron vortex does not conserve its OAM while propagating through a crystal, as the free space cylindrical symmetry is broken by the crystal potential [14,15,16]. The probing electron in the crystal is therefore not in a quantum mechanical state with well-defined OAM during its propagation and parts of it acquire different OAM, reducing the intensity of the $\pm\hbar$ components and, in turn, the dichroic signal [17]. Third, it is experimentally challenging to prepare a high-quality coherent atomic size electron vortex beam. [8]

These drawbacks can be solved if a standard electron probe can be used and post interaction analysis in terms of OAM can be performed on the inelastically scattered electrons, as proposed in Ref. [18] for amorphous materials. Accordingly, here we propose a new approach for performing EMCD experiments based on post-selection in both energy and OAM of inelastically scattered electrons from a crystalline magnetic sample. The proposed setup is shown schematically in Figure 1.

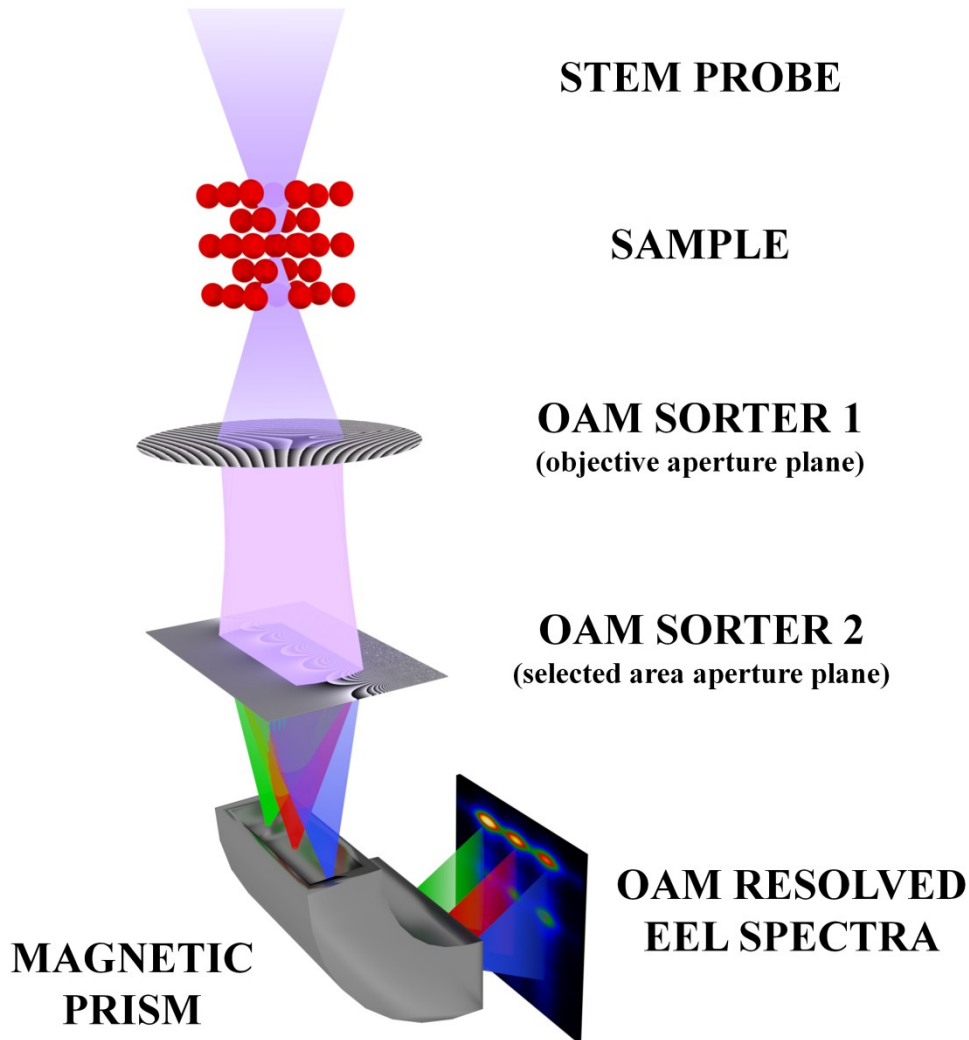


Figure 1: Proposed experimental setup needed to perform an OAM-resolved electron energy-loss (EEL) spectroscopy experiment in a scanning TEM (STEM).

A conventional focused electron probe, which has been formed using a circular aperture, is used to image a magnetic sample along a high symmetry zone axis. Two phase elements (referred to as

OAM sorters) [19, 20, 21], which are located in the objective and selected area diffraction planes of the microscope column, are used to spatially separate the OAM components of the electron beam. If these elements have an appropriate orientation, then the electrons can be analyzed using an energy-selecting spectrometer to achieve double dispersion of the electrons (in orthogonal directions) in both energy and OAM [22].

In contrast to the use of an electron vortex beam as a probe, this setup allows the two spectra that are needed for an EMCD measurement to be recorded simultaneously. Furthermore, the sample can be oriented along a high symmetry direction, allowing for atomic resolution. In addition, as we explain below, the approach increases the SNR, as a large fraction of the inelastic signal is used to record the EMCD spectra.

Theory

We begin by describing the theory that is required to simulate OAM-resolved core loss spectra $I(l, \Delta E)$ in crystalline samples using multislice calculations. Interestingly, the formalism that is required to describe EMCD spectra becomes clearer once a description in terms of electronic OAM is used, when compared to a description in terms of linear momentum.

The combined use of OAM sorters and an EEL spectrometer provides access to the quantities

$$I(l, \Delta E) = \text{Tr}[\hat{\rho}_f \hat{P}_{lE}], \quad (1)$$

where $\hat{\rho}_f$ is the electron density matrix after passing the sample, $\hat{P}_{lE} = \int dk |l, k, E\rangle \langle l, k, E|$ and $E = E_0 - \Delta E$ is the energy of an electron that has lost energy ΔE . The quantum states $|l, k, E\rangle$ are characterized by OAM values $\hbar l$ and energies E , while k is a quantum number whose physical meaning is explained below. The quantity $I(l, \Delta E)$, which is experimentally available using the proposed setup, defines the number of electrons that have energy $E_0 - \Delta E$ and are found in a state with OAM equal to $\hbar l$. The dichroic signal can be obtained as a difference between $I(+1, \Delta E)$ and $I(-1, \Delta E)$.

We make use of the approach described in Ref. [23] to simulate OAM-resolved core loss spectra. We adapt the procedure, which is reviewed here for completeness, from a momentum-defined to an angular-momentum-defined final state basis, based on the following approximations:

- The electrons are assumed to undergo single inelastic processes while passing through the sample. This approximation is justified by the low probability of core loss excitation.
- The energy of the probing electrons is assumed to be 300 keV. We work in the paraxial approximation, for which the electron wavefunction can be written $\Psi(\mathbf{r}) = e^{ik_z z} \phi(\mathbf{r}^\perp; z)$, where we use the definition $\phi(\mathbf{r}^\perp; z) \equiv \langle \mathbf{r}^\perp | \phi_z \rangle$ below for the transverse wavefunction at height z ;
- We use the z -locality approximation [24, 25], where the state of an electron after inelastic scattering from an atom located at \mathbf{a} can be written $|\phi_{z=z_a}^{f_a}\rangle = -i\sigma \hat{V}_{i \rightarrow f}^{proj} |\phi_{z=z_a}^{el}\rangle$, the atom at \mathbf{a} experiences a transition $|i\rangle \rightarrow |f\rangle$, $|\phi_{z=z_a}^{el}\rangle$ is the electron state at $z = z_a$ before inelastic scattering, $\hat{V}_{i \rightarrow f}^{proj}$ is defined in Eq. 4 in Ref. [23] and σ is a parameter that depends only on the energy of the electron beam.
- We consider a highly symmetrical cubic crystal, *i.e.*, *bcc* iron. This assumption simplifies the definitions of the quantities of interest. However, the conclusions that we obtain for this system can be generalized to less symmetrical samples.

We define $I(l, \Delta E)$ as follows:

$$I(l, \Delta E) = \int_0^{K_{Max}} I(l, k, \Delta E) dk , \quad (2)$$

where

$$I(l, k, \Delta E) = \sum_{a,f} |\langle l, k | \phi_{z=z_a}^{f_a} \rangle|^2 \delta(\Delta E + \varepsilon_f - \varepsilon_i) . \quad (3)$$

The states $|l, k \rangle$ are defined such that $\langle \mathbf{r}^\perp | l, k \rangle = e^{il\varphi} J_{|l|}(k|\mathbf{r}^\perp|)$, *i.e.*, they correspond to Bessel beams with orbital angular momentum l and transverse wavevector k . The integral over k in Eq. 2 is performed up to $K_{Max} = 2\pi\alpha/\lambda$, where α is the numerical aperture of the OAM sorter in the back focal plane of the objective lens, while λ is the electron de Broglie wavelength, which takes a value of 1.97 pm at 300 kV.

Proceeding as in Ref. [23], it is possible to rewrite $I(l, k, \Delta E)$ as a superposition integral of the probe propagating in the sample and a counter-propagating wave from a single state of the detector for defined values of l, k , according to the expression

$$I(l, k, \Delta E) = \sigma^2 \sum_{\mathbf{a}} \int d\mathbf{k}_1 \dots \int d\mathbf{k}_4 D^*(\mathbf{k}_1; l, k) C(\mathbf{k}_2) D(\mathbf{k}_3; l, k) C^*(\mathbf{k}_4) \frac{S_{\mathbf{a}}(\tilde{\mathbf{q}}, \tilde{\mathbf{q}}', \Delta E)}{\tilde{q}^2 \tilde{q}'^2} e^{i(\mathbf{q}-\mathbf{q}')\mathbf{a}} , \quad (4)$$

where the sum over \mathbf{a} is performed over atomic positions at which the inelastic process of interest can occur. Given the infinitesimal distribution in k , $D(\mathbf{k}_1; l, k)$ is the three-dimensional Fourier transform of an elastically scattered Bessel beam with topological charge l , transverse wavevector k and energy $E_0 - \Delta E$ propagating from the bottom to the top of the crystal. This new definition of $D(\mathbf{k}_1; l, k)$ is one of the innovative additions to the present numerical simulation approach.

In this expression, the energy dependence of $D(\mathbf{k}_1; l, k)$ is neglected, as we focus on a small range of energy losses ΔE in the interval $[\Delta E_{min}, \Delta E_{max}] = [690, 750]$ eV. The propagation of an electron of energy $E_0 - \Delta E_{min}$ is similar to that of one with energy $E_0 - \Delta E_{max}$ because $E_0 \gg \Delta E_{max}, \Delta E_{min}$.

Analogously, $C(\mathbf{k}_2)$ is the three-dimensional Fourier transform of an incident beam that propagates elastically in the material with energy E_0 . Both $D(\mathbf{k}_1; l, k)$ and $C(\mathbf{k}_2)$ can be obtained by performing three-dimensional Fourier transforms of the wavefunction inside the crystal, computed using a multislice calculation. We also have the expressions

$$\tilde{\mathbf{q}} = \mathbf{k}_1^\perp - \mathbf{k}_2^\perp + q_{\Delta E} \hat{\mathbf{z}} \quad \tilde{\mathbf{q}}' = \mathbf{k}_3^\perp - \mathbf{k}_4^\perp + q_{\Delta E} \hat{\mathbf{z}}$$

$$\mathbf{q} = \mathbf{k}_1 - \mathbf{k}_2 \quad \mathbf{q}' = \mathbf{k}_3 - \mathbf{k}_4$$

$$q_{\Delta E} = k_z^f - k_z^i .$$

In Eq. 4, $S_{\mathbf{a}}(\tilde{\mathbf{q}}, \tilde{\mathbf{q}}', \Delta E)$ is the atomic mixed dynamic form factor [26], which provides the energy dependence of $I(l, k, \Delta E)$. Working within the dipolar approximation, we can write [27]

$$S_{\mathbf{a}}(\tilde{\mathbf{q}}, \tilde{\mathbf{q}}', \Delta E) = \tilde{\mathbf{q}} \mathbb{N}_{\mathbf{a}}(\Delta E) \tilde{\mathbf{q}}' + i \mathcal{M}_{\mathbf{a}}(\Delta E) [\tilde{\mathbf{q}} \times \tilde{\mathbf{q}}'] ,$$

where $\mathcal{M}_a(\Delta E)$ is a vector that describes the magnetic properties of the sample, while $\mathbb{N}_a(\Delta E)$ is a real symmetric tensor, taking into account the non-magnetic contributions to the signal. We assume that the magnetic field of the objective lens is sufficiently strong to saturate the magnetization in the sample along z . Only the z component of $\mathcal{M}_a(\Delta E)$ is then non-zero. For a cubic crystal whose axes are parallel to \hat{x} , \hat{y} and \hat{z} , $\mathbb{N}_a(\Delta E)$ becomes a diagonal tensor, with all of the diagonal elements equal to each other. We now introduce a set of functions [28] that allow us to group together the different terms that are associated with dynamical diffraction effects. We define

$$Q_a^i(l, k) = \sigma \int d\mathbf{k}_1 \int d\mathbf{k}_2 D^*(\mathbf{k}_1; l, k) C(\mathbf{k}_2) \frac{\hat{q}_i}{\hat{q}^2} \quad i = x, y, z \quad (5)$$

$$X_i(l, k) = \sum_a |Q_a^i(l, k)|^2 \quad (6)$$

$$S(l, k) = -2\text{Im}[\sum_a Q_a^x(l, k) Q_a^y(l, k)^*] . \quad (7)$$

We then have the expression

$$I(l, k, \Delta E) = \sum_{i=x,y,z} N_i(\Delta E) X_i(l, k) + \mathcal{M}(\Delta E) S(l, k) , \quad (8)$$

where we have neglected the dependence of \mathbb{N} and \mathcal{M} on atom type, as we focus on energy losses produced by atoms of the same type and the same coordination geometry in the crystal. The functions $X_i(l, k)$ and $S(l, k)$ describe the effect of dynamical diffraction in the crystal and need to be tuned to achieve optimal experimental conditions.

By exploiting the cubic symmetry of the crystal, we can define a relative dichroism function at fixed k of the form

$$R(\Delta E, k) = 100 \times \frac{\mathcal{M}(\Delta E)}{N(\Delta E)} \frac{|S(l, k)|}{\sum_i X_i(l, k)} \approx 25 \times \frac{|S(l, k)|}{\sum_i X_i(l, k)} .$$

The ratio $\frac{\mathcal{M}(\Delta E)}{N(\Delta E)}$ depends on the electronic structure of the material and should be calculated using density functional theory. For strong ferromagnets, it is typically close to 25% [29,30] and represents the maximum expected dichroic signal.

In order to relate the above functions to quantities that can be measured experimentally, Eq. 8 must be integrated over the interval $[0; K_{Max}]$. Under general assumptions and using the definitions in Eqs 6 and 7, it is possible to show that $X_i(l, k) = X_i(-l, k)$ and $S(l, k) = -S(-l, k)$ (see the Appendix). Integrating over k , we find that

$$I(l, K_{Max}, \Delta E) = N(\Delta E) \sum_{i=x,y,z} X_i(l, K_{Max}) + \mathcal{M}(\Delta E) S(l, K_{Max}) . \quad (9)$$

For $l = \pm 1$, we obtain the expressions

$$I(+1, \Delta E; K_{Max}) - I(-1, \Delta E, K_{Max}) = 2\mathcal{M}(\Delta E) |S(+1, K_{Max})|$$

and

$$I(+1, \Delta E, K_{Max}) + I(-1, \Delta E, K_{Max}) = 2 \sum_i N_i(\Delta E) X_i(+1, K_{Max}) ,$$

from which the dichroism function can be defined as

$$D(\Delta E; K_{Max}) = 100 \times \frac{\mathcal{M}(\Delta E) |S(+1, K_{Max})|}{\max [N(\Delta E) \sum_i X_i(+1, K_{Max})]} . \quad (10)$$

This function describes the strength of the dichroic signal and depends on the collection semi-angle chosen for the experiment. Below, we present the behavior of these functions and outline a possible strategy to select an appropriate value for the collection semi-angle.

Results

In this section, we present calculations of the non-magnetic signal $X_i(l, k)$ and the magnetic signal $S(l, k)$ for $l = [-2: 2]$ and different values of k for *bcc* Fe oriented along the [001] direction. In the simulations, we use an orthogonal supercell of size $[20 \times 20 \times 140]a$ (where $a=0.287$ nm is the lattice parameter of Fe), corresponding to an overall sample thickness of 40 nm. The electron probe has a convergence semi-angle of 7.3 mrad (in agreement with the experimental setup used in Ref. [19]) and is centered on an Fe column at (0,0). The signals $X_i(l, k)$ and $S(l, k)$ are evaluated by summing the products $D^*(\mathbf{k}_1; l, k)C(\mathbf{k}_2)$ using a modified version of the software MATSv2 [28] for a convergence parameter of $5 \cdot 10^{-9}$.

Figure 2a shows the magnetic term $S(l, k)$ for different values of l . In agreement with the conclusions reported in the Appendix (*i.e.*, $S(l, k) = -S(-l, k)$), for $l = +1$ this function is equal in modulus but opposite in sign to that evaluated for the opposite topological charge and is zero if the orbital angular momentum is taken to be zero. It is also negligible for larger values of $|l|$, meaning that electrons collected for $l = \pm 1$ are good candidates for obtaining information about the magnetic properties of the sample. Figure 2b shows the non-magnetic term $\sum_i X_i(l, k)$, which is non-zero for $l = 0$. It decreases more rapidly than the non magnetic contribution for $l = \pm 1$ and is peaked at smaller scattering angles (λk). In contrast to the magnetic terms, these quantities are independent of the sign of the OAM (as $\sum_i X_i(1, k) = \sum_i X_i(-1, k)$), while they become negligible for $|l| > 2$.

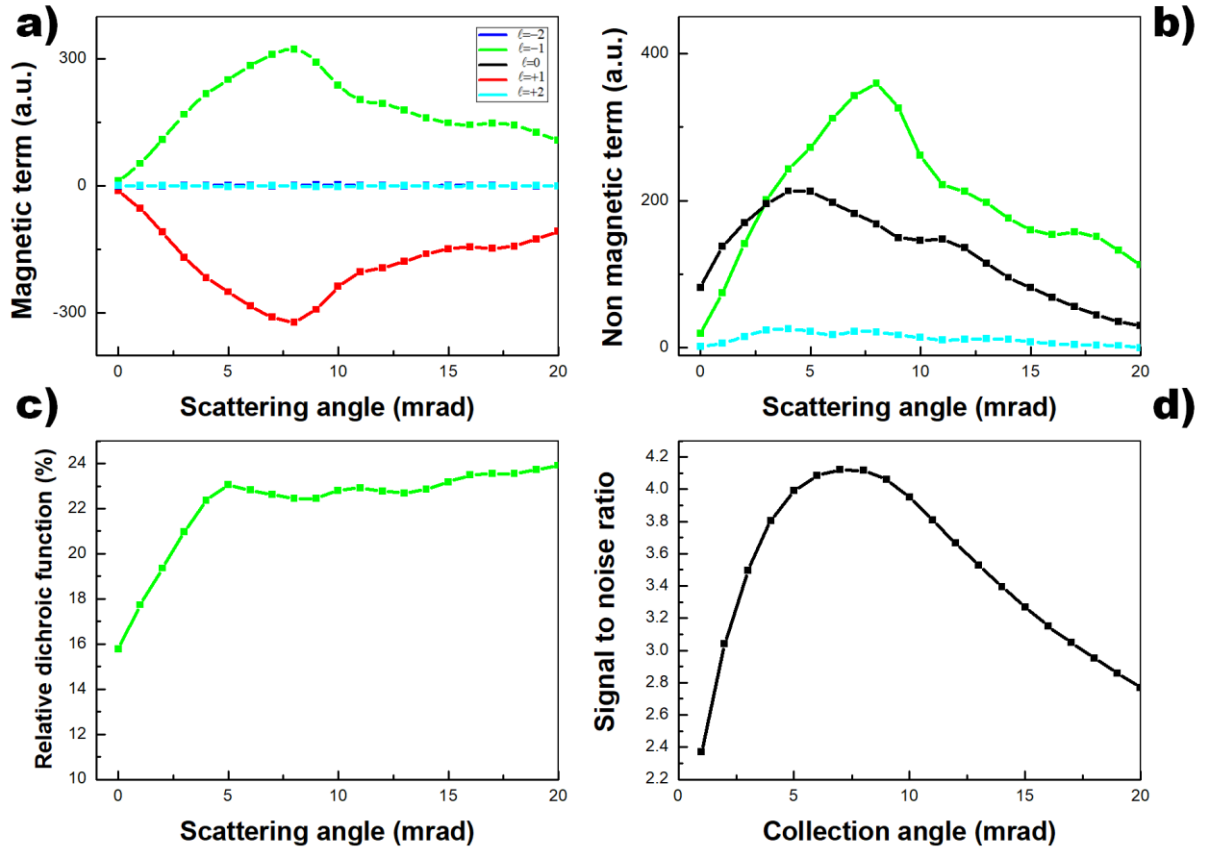


Figure 2: a) Magnetic $S(l, \mathbf{k})$ and b) non-magnetic $\sum_i X_i(l, \mathbf{k})$ terms plotted vs transverse wavevector length \mathbf{k} for l in the interval $[-2; +2]$. c) Relative dichroic function $R(\Delta E, \mathbf{k})$ plotted vs scattering angle $\lambda \mathbf{k}$. d) Figure of merit function (defined in Eq. 11) for an optimal value of the maximum collection semi-angle to maximize the magnetic signal.

Figure 2c shows the relative dichroic function $R(\Delta E, k)$ plotted for $l = -1$ in the λk interval $[0; 20]$ mrad. This function takes values well above 15% over this entire interval, approaching the theoretical limit of 25% for scattering angles exceeding 5 mrad.

These trends confirm the need to properly choose the collection semi-angle to maximize the magnetic signal. We now define a figure of merit, which can be used to determine a value of K_{Max} for which the magnetic signal (at a given $l = \pm 1$) is maximized with respect to the non-magnetic signal, taking into account the fact that an increase in the overall collection semi-angle decreases the SNR, making this experimental configuration less advantageous.

A reasonable figure of merit is given by the expression [29,31]

$$F(K_{Max}) = \frac{1}{K_{Max}} \frac{|S(|l|, K_{Max})|}{\sqrt{\sum_i X_i(|l|, K_{Max})}}, \quad (11)$$

where the ratio between the magnetic and non-magnetic terms is analogous to the SNR in Ref. [32], the magnetic contribution is the “signal” that should be optimized and $\sum_i X_i(|l|, K_{Max})$ is the “noise” to be decreased. The function $1/K_{Max}$ describes the increase in SNR that we expect to observe on enlarging the collection semi-angle. [29] In the present calculations, this function (shown in Fig. 2d) has maximum values in the range $[5; 7]$ mrad, suggesting that these angles are appropriate collection semi-angles to be used for this material.

It is important to understand if the approach described here provides access to magnetic properties with atomic spatial resolution. According to the definition of $S(l, k)$ in Eq. 7, the sum is performed over all of the magnetic atoms in the sample, not only those in the column on which the STEM probe is focused. In order to clarify this point, we evaluated the contributions to the magnetic signal (Figs 3a and 3c) and the non-magnetic signal (Fig. 3b and 3d) for $l = +1$ for both the atoms in the column on which the probe is centered and those in the neighboring columns [28, 32]. The magnitudes of the terms are represented as solid spheres centered on each atomic position. The radius of each sphere is directly proportional to the modulus of that term. The same information is encoded in the spheres' colors on a logarithmic scale (see color bars in Fig. 3). The contributions decrease rapidly for atoms that are not on the column centered at the origin, suggesting that the measured signal comes almost entirely from the atomic column of interest. Atomic spatial resolution in measuring the magnetic properties of the material is therefore expected.

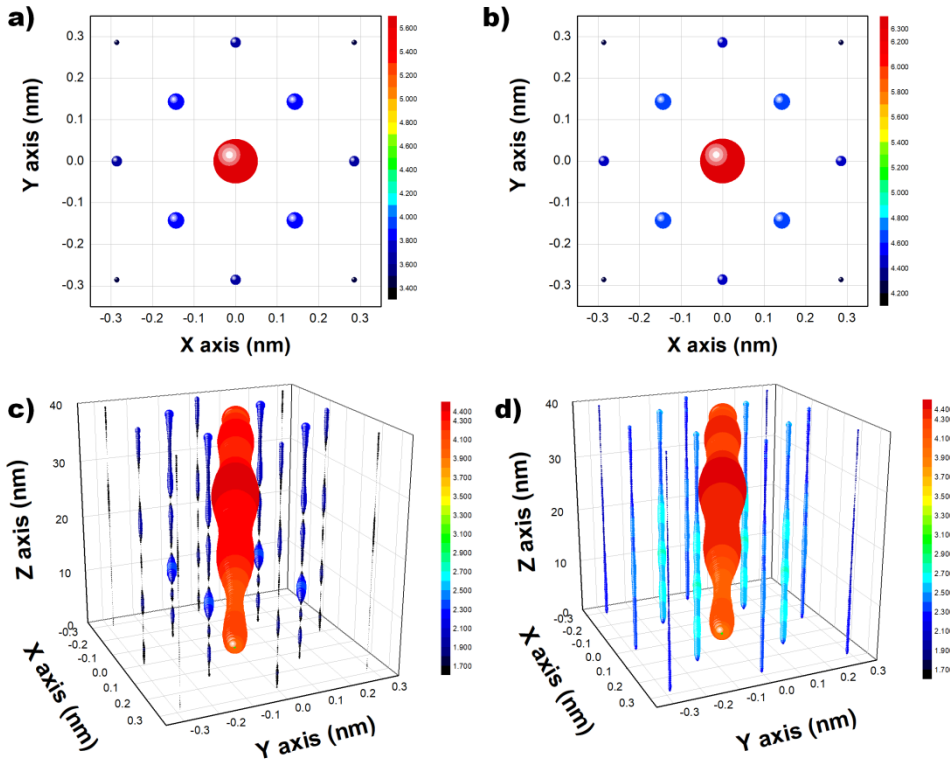


Figure 3: a) and c) Two-dimensional and three-dimensional views, respectively, of contributions to the function $S(+1, \lambda K_{Max} = 7 \text{ mrad})$ from atoms close to and on the atomic column on which the electron probe is centered. Each atom is surrounded by a sphere, whose radius (and color, on a logarithmic scale) is proportional to the strength of the contribution from that atom. On increasing the distance from the atomic column at (0, 0), there is a rapid decrease in the contribution from the atoms to S . b) and d) Corresponding depictions for the non-magnetic part of the signal.

Once the functions that describe dynamical diffraction of the electron beam in the sample are known, it is possible to estimate OAM-resolved EEL spectra using Eq. 9. The functions $N(\Delta E)$ and $\mathcal{M}(\Delta E)$ have been evaluated using first principles calculations [3, 32], while the maximum collection angle was fixed to 7 mrad. First principles calculations were performed for *bcc* Fe using the WIEN2k package [33] using the generalized gradient approximation for the exchange-correlation functional [34] and including spin-orbit coupling effects. The atomic sphere radius of Fe was set to 2.33 Bohr radii, the basis size cut-off was $RK_{max} = 8.0$ and Brillouin zone integrations were performed using a modified tetrahedron method with 10000 \mathbf{k} points. The upper panel of Fig. 4a shows the resulting spectra for different values of OAM, while lower panel shows the dichroic function defined in Eq. 10. The quantity $D(\Delta E; \lambda K_{Max} = 7 \text{ mrad})$ reaches values of $\sim 15\%$

(or more) at both the L_2 and the L_3 Fe edges. This quantity is much larger than the relative dichroic signal that is observed using conventional approaches to EMCD.

As outlined above, this approach should provide access to double dispersion, in perpendicular directions, as a function of energy and orbital angular momentum. However, in reality the spectra shown in Fig. 4a are different from those that we expect to measure. In order to obtain results that are similar to those expected from a real life experiment, our treatment must include broadening in energy of the electron beam (as it is not perfectly monochromatic) and finite energy resolution of the OAM sorters. What we expect to observe in practice is

$$\Gamma(l, \Delta E) = I(l, \Delta E) \otimes f(l, \Delta E) , \quad (12)$$

where $f(l, \Delta E)$ is the product of two Gaussian functions describing broadening introduced by the experimental setup. The OAM is treated as a continuous variable, since the sorter can transform a vortex with topological charge l in a spot centered at coordinate C/l [19, 20, 21] with a lateral extension equal to $C\Delta l$ (where C is a constant that depends on the sorter parameters and is assigned a value of unity for simplicity in the images presented in the main text).

Figure 3b shows the result of this convolution procedure for $\Delta l = 0.5\hbar$ and $\Delta E = 0.7\text{eV}$, as this is the resolution expected using a sorter in a fan-out configuration, as recently demonstrated for optical sorters [35]. Despite the finite OAM resolution, which introduces partial mixing of the signal at $l = 0$ with that for $l = \pm 1$, strong asymmetry between $\Gamma(+1, \Delta E)$ and $\Gamma(-1, \Delta E)$ is observable.

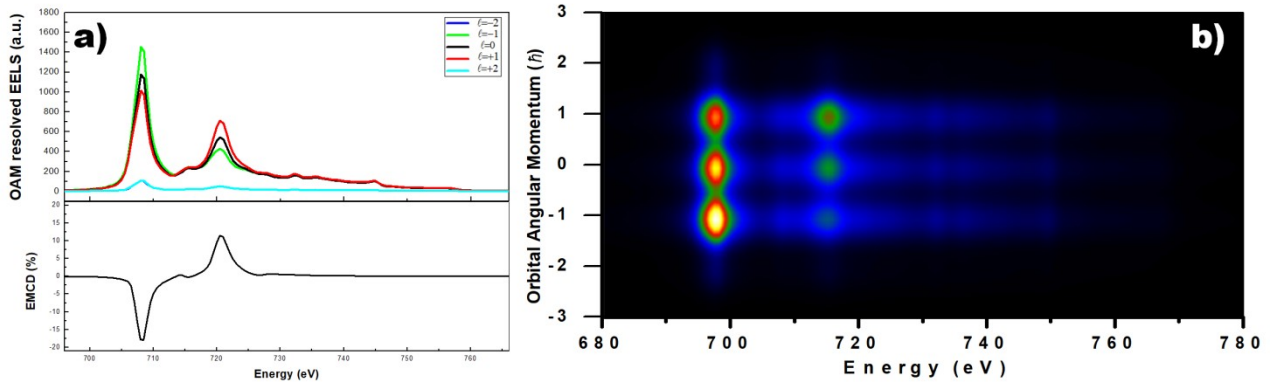


Figure 4: a) Upper panel: OAM-resolved EEL spectra computed for l in the range $[-2; +2]$ for a collection semi-angle of 7 mrad. Lower panel: $D(\Delta E)$ defined in Eq. 10, in which the dichroism strength reaches values of $\sim 18\%$ for both the L_2 and the L_3 edge of Fe. b) Convolution of the spectra shown in a) with the product of two Gaussian functions describing broadening in OAM ($0.5\hbar$) and energy (0.7 eV) introduced by the OAM sorters and non-monochromaticity of the electron beam.

It should be noted that the inelastic signal that we observe for $l = \pm 2$ is not due to electron transitions with a change in OAM equal to $\pm 2\hbar$, as our approach is based on a dipolar approximation, but it is only due to a lack of OAM conservation for a beam that propagates in a crystal. More precisely, once an electron has experienced an inelastic event, it keeps propagating in the crystal but its OAM is not conserved and acquires components corresponding to $l \neq 0, \pm 1$ (e.g., for $l = \pm 2$), giving rise to a non-zero signal.

Figure 5 shows in-plane spatial mapping of the dichroic function $D(\Delta E; \lambda K_{Max} = 7 \text{ mrad})$ obtained by computing OAM-resolved EEL spectra following the procedure outlined above, but scanning the STEM probe across the sample. In Figs 5a and 5b, the function is computed for the L_2 and L_3 edges,

respectively, at energies of $\Delta E = 720$ and 708 eV. In absolute value, the strength of the relative dichroism is maximum when the electron beam is centered on an atomic column for both edges, whereas it decreases by a factor of two when the probe is moved between columns, thereby providing information about the magnetic properties of the sample with atomic spatial resolution.

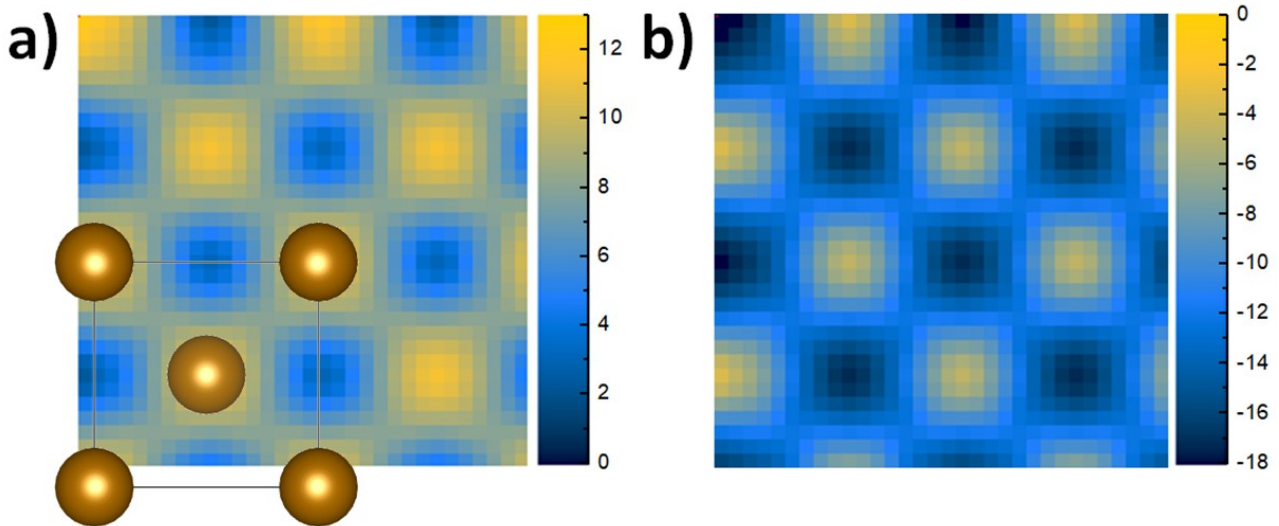


Figure 5: Spatial mapping of the function $D(\Delta E; \lambda K_{Max} = 7 \text{ mrad})$ computed for the Fe a) L_2 and b) L_3 edges. The contrast in the images provides access to atomically resolved mapping of magnetic properties of the sample.

Conclusions

We report a new approach that can be used to probe electron magnetic chiral dichroism in the transmission electron microscope by exploiting the recently demonstrated capability of evaluating the orbital angular momentum spectrum of an electron beam. By focusing on the simple case of *bcc* Fe, we introduce the required theoretical framework and outline a possible approach to maximize the magnetic signal. Our results show that this approach should provide strong dichroic signals with atomic spatial resolution, even without requiring very high resolution in orbital angular momentum. It also has the great advantage of maximizing the ratio of magnetic to non-magnetic component of the inelastic electron signal, thereby increasing the signal to noise ratio.

Funding Sources

This work is supported by Q-SORT, a project funded by the European Union's Horizon 2020 Research and Innovation Program under grant agreement No. 766970.

Appendix

In this appendix, we demonstrate the following properties:

- $S(l, k) = -S(-l, k)$;
- $X_i(l, k) = X_i(-l, k)$

Assuming that the crystalline potential satisfies the symmetry operation

$$V(x, y, z) = V(-x, y, z) . \quad (\text{A1})$$

We begin by explicitly writing the function $D(\mathbf{k}_1; l, k)$ in the form

$$D(\mathbf{k}_1; l, k)^* = \int dz e^{izk_1^z} \int d\mathbf{r}_\perp e^{i\mathbf{k}_1^\perp \cdot \mathbf{r}_\perp} [U^+(\mathbf{r}_\perp, z) e^{il\varphi} J_{|l|}(k|\mathbf{r}^\perp|) e^{-izk_f}]^* , \quad (\text{A2})$$

where $U(\mathbf{r}_\perp, z)$ is an evolution operator defined in Ref. [23] and k_f is the projection along the z axis of the wave vector of the inelastically scattered electron. The operator $U(\mathbf{r}_\perp, z)$ is invariant under symmetry operations of the crystal, so in our case

$$U(x, y, z) = U(-x, y, z) . \quad (\text{A3})$$

By performing the substitution $x \rightarrow -x'$ in Eq. A2, exploiting Eq. A3 and remembering that

$$\int_{-\infty}^{+\infty} dx \rightarrow \int_{+\infty}^{-\infty} -dx' = \int_{-\infty}^{+\infty} dx'$$

$$\varphi = \text{atan} \frac{y}{x} \rightarrow \varphi' = \text{atan} \frac{y}{-x'} = -\varphi$$

$$J_{|l|}(k|\mathbf{r}^\perp|) = J_{|-l|}(k|\mathbf{r}^\perp|) ,$$

we find that

$$D(\mathbf{k}_1; l, k)^* = \int dz e^{izk_1^z} \int dx' dy e^{-ik_1^x x'} e^{ik_1^y y} [U^+(-x', y, z) e^{-il\varphi} J_{|l|}(k|\mathbf{r}^\perp|) e^{-izk_f}]^* = D(-k_1^x, k_1^y, k_1^z; -l, k)^* .$$

Using this relation in the definition of $Q_a^x(l, k)$ results in the expression

$$Q_a^x(l, k) = \int d\mathbf{k}_1 \int d\mathbf{k}_2 D(-k_1^x, k_1^y, k_1^z; -l, k)^* C(\mathbf{k}_2) \frac{k_1^x - k_2^x}{\tilde{q}^2} e^{iqa} , \quad (\text{A4})$$

which (with the substitutions $-k_1^x \rightarrow k_1'^x$ and $-k_2^x \rightarrow k_2'^x$) can be rewritten

$$Q_a^x(l, k) = - \int d\mathbf{k}'_1 \int d\mathbf{k}'_2 D(k_1'^x, k_1'^y, k_1'^z; -l, k)^* C(-k_2'^x, k_2'^y, k_2'^z) \times \frac{k_1'^x - k_2'^x}{\tilde{q}^2} e^{-i(k_1'^x - k_2'^x)a_x} e^{i(k_1'^y - k_2'^y)a_y} e^{i(k_1'^z - k_2'^z)a_z} \quad (\text{A5})$$

from which it is apparent that $Q_{a_x a_y a_z}^x(l, k) = -Q_{-a_x a_y a_z}^x(-l, k)$.

By proceeding in the same manner, it is possible to show that $Q_{a_x a_y a_z}^y(l, k) = Q_{-a_x a_y a_z}^y(-l, k)$ and $Q_{a_x a_y a_z}^z(l, k) = Q_{-a_x a_y a_z}^z(-l, k)$. Therefore, using the definition of $S(l, k)$, we have

$$S(l, k) = -2Im \left[\sum_{\mathbf{a}} Q_{a_x a_y a_z}^x(l, k) Q_{a_x a_y a_z}^y(l, k)^* \right] = 2Im \left[\sum_{\mathbf{a}} Q_{-a_x a_y a_z}^x(-l, k) Q_{-a_x a_y a_z}^y(-l, k)^* \right] = -S(-l, k) ,$$

where we have exploited the fact that, because of Eq. A1, if we have an atom at position $(a_x a_y a_z)$ then we will have an analogous atom at position $(-a_x a_y a_z)$. By the same reasoning, $X_i(l, k) = X_i(-l, k)$ for $i = x, y, z$.

References

-
- [1] P. Schattschneider, S. Rubino, C. Hebert, J. Rusz, J. Junes, P. Kovak, E. Carlino, M. Fabrizioli, G. Panaccione and G. Rossi, *Nature* **441**, 486 (2006).
- [2] D. Song, Z. Wang and J. Zhu *Ultramicroscopy*, **201**, 1-17, (2019).
- [3] J. Rusz, S. Rubino and P. Schattschneider, *Phys. Rev.B*, **75**, 214425 (2007).
- [4] P. Schattschneider, C. Herbert, S. Rubino, M. Stoger-Pollach, J. Rusz, P. Novak, *Ultramicroscopy* **108** 433-438 (2008).
- [5] J. Verbeeck, H. Tian and P. Schattschneider, *Nature* **467**, 301-304 (2010).
- [6] M. Uchida and A. Tonomura, *Nature* **464**, 737-739 (2010).
- [7] B.J. McMorran, A. Agrawal, I.M. Anderson, A.A. Herzing, H.J. Lezec, J.J. McClelland and J. Unguris, *Science* **331**, 192-195 (2011).
- [8] D. Pohl, S. Schneider, P. Zeiger, J. Rusz, P. Tiemeijer, S. Lazar, K. Nielsch and B. Rellinghaus, *Scientific Reports* **7**, 934 (2017).
- [9] A. B  ch  , R. Juchtmans and J. Verbeeck, *Ultramicroscopy* **178**, 12-19, (2017)
- [10] R. Van Boxem, B. Partoens and J. Verbeeck, *Phys. Rev. A* **91**, 032703 (2015).
- [11] J. Rusz and S. Bhowmick, *Phys. Rev. Lett.* **111**, 105504 (2013).
- [12] J. Rusz, J-C. Idrobo and S. Bhowmick, *Phys. Rev. Lett.* **113**, 145501 (2014).
- [13] J. Rusz, J-C. Idrobo and L. Wrang, *Phys. Rev. B* **94**, 144430 (2016).
- [14] E. J. Kirkland, *Advanced Computing in Electron Microscopy*, 2nd ed. (Springer, New York, 2010).
- [15] S. Loffler and P. Schattschneider, *Acta Cryst. A* **68**, 443-447 (2012).
- [16] B.G. Mendis, *Ultramicroscopy* **149**, 74-85(2015).
- [15] J. Rusz, S. Bhowmick, M. Eriksson and N. Karlsson, *Phys. Rev. B* **89**, 134428 (2014).
- [18] T. Schachinger, S. L  ffler, A. Steiger-Thirsfeld, M. St  ger-Pollach, S. Schneider, D. Pohl, B. Rellinghaus and P. Schattschneider, *Ultramicroscopy*, **179**, 15-23 (2017).
- [19] V. Grillo, A.H. Tavabi, F. Venturi, H. Larocque, R. Balboni, G.C. Gazzadi, S. Frabboni, P.H. Lu, E. Mafakheri, F. Bouchard, R.E. Dunin-Borkowski, R.W. Boyd, M.P.J. Lavery, M.J. Padgett and E. Karimi, *Nature Communications* **8**, 15536 (2017).
- [20] B.J. McMorran, T.R. Harvey and M.P.J. Lavery, *New J. Phys.* **19**, 023053 (2017).
- [21] G.C.G. Berkhout, M.P.J. Lavery, J. Courtial, M. Beijersbergen and M.J. Padgett, *Phys. Rev. Lett.* **105**, 153601 (2010).
- [22] M. Zanfrognini, E. Rotunno, S. Frabboni, A. Sit, E. Karimi, U. Hohenester and V. Grillo, *ACS Photonics* **6**, 620 (2019).
- [23] J. Rusz, A. Lubk, J. Spiegelberg and D. Tyutynnikov, *Phys. Rev. B* **96**, 245121 (2017).
- [24] C. Dwyer, *Ultramicroscopy* **104**, 141 (2005).
- [25] J. Verbeeck, P. Schattschneider and A. Rosenauer, *Ultramicroscopy* **109**, 350 (2009).
- [26] H. Kohl and H. Rose, *Adv. Electron. Electron Phys.* **65**, 173 (1985).
- [27] J. Rusz, S. Rubino, O. Eriksson, P.M. Oppeneer and K. Leifer, *Phys.Rev.B* **84**, 064444 (2011).
- [28] J. Rusz, *Ultramicroscopy* **177**, 20-25 (2017).
- [29] J. Rusz and J.C. Idrobo *Phys. Rev. B* **93**, 104420 (2016).
- [30] A. Ankudinov and J. Rehr, *Phys. Rev. B* **51**, 1282 (1995)
- [31] S. L  ffler and W. Hetaba, *Microscopy*, **67**, 60-71 (2018).
- [32] D.S. Negi, J.C. Idrobo and J. Rusz, *Scientific Reports* **8**, 4019 (2018).
- [33] P. Blaha, K. Schwarz, G.K.H. Madsen, D. Kvasnicka, J. Luitz, R. Laskowski, F. Tran and L.D. Marks, WIEN2k, An Augmented Plane Wave + Local Orbitals Program for Calculating Crystal Properties (Karlheinz Schwarz, Techn. Universit  t Wien, Austria), 2018. ISBN 3-9501031-1-2.
- [34] J.P. Perdew, K. Burke and M. Ernzerhof, *Phys. Rev. Lett.* **77**, 3865 (1996).

[35] M. Mirhosseini, M. Malik, Z. Shi and R.W. Boyd, *Nature Communications* **4**, 2783 (2013).